nature geoscience

LETTERS

PUBLISHED ONLINE: 7 DECEMBER 2015 | DOI: 10.1038/NGEO2599

Sub-micrometre particulate matter is primarily in liquid form over Amazon rainforest

Adam P. Bateman[1], Zhaoheng Gong[1], Pengfei Liu[1], Bruno Sato[2], Glauber Cirino[3], Yue Zhang[1], Paulo Artaxo[4], Allan K. Bertram[5], Antonio O. Manzi[3], Luciana V. Rizzo[6], Rodrigo A. F. Souza[7], Rahul A. Zaveri[8] and Scot T. Martin[1,9]*

Atmospheric particulate matter influences the Earth's energy balance directly, by altering or absorbing solar radiation, and indirectly by influencing cloud formation[1]. Whether organic particulate matter exists in a liquid, semi-solid, or solid state can affect particle growth and reactivity[2,3], and hence particle number, size and composition. The properties and abundance of particles, in turn, influence their direct and indirect effects on energy balance[4]. Non-liquid particulate matter was identified over a boreal forest of Northern Europe[5], but laboratory studies suggest that, at higher relative humidity levels, particles can be liquid[6,7]. Here we measure the physical state of particulate matter with diameters smaller than 1 μm over the tropical rainforest of central Amazonia in 2013. A real-time particle rebound technique shows that the particulate matter was liquid for relative humidity greater than 80% for temperatures between 296 and 300 K during both the wet and dry seasons. Combining these findings with the distributions of relative humidity and temperature in Amazonia, we conclude that near-surface sub-micrometre particulate matter in Amazonia is liquid most of the time during both the wet and the dry seasons.

Particulate matter (PM) can occur in liquid (viscosity $<10^2$ Pa s), semi-solid (10^2–10^{12} Pa s) and solid ($>10^{12}$ Pa s) states[8]. By influencing molecular diffusion within the particle, the physical state affects the rates and pathways of atmospheric processing of PM, with consequent influences on particle growth rates[9] as well as cloud condensation[10] and ice nuclei efficiencies[11]. Under clean conditions in forested environments, PM in the climate-relevant sub-micrometre-size domain is produced in large part by the oxidation of biogenic volatile organic compounds (BVOCs; refs 12,13). This organic PM was assumed until recently to be liquid. A liquid state tends to favour the growth of larger particles because of the rapid absorption of semi-volatile organic vapours, thereby suppressing the growth of smaller particles[14,15]. In a study of organic PM in a boreal forest of Northern Europe, however, Virtanen *et al.*[5] suggested that PM is semi-solid or solid. That study led to doubts about the appropriateness of liquid-oriented process algorithms implemented in traditional chemical transport models (CTMs). These models are used to predict the number and mass concentrations of PM underlying many climate-related effects[14]. Many laboratory[2,3,6,7,16–18] and modelling[15,19] studies were subsequently motivated. A species diffusivity of 10^{-15} cm^2 s^{-1} within PM has been proposed as a threshold value above which particle-phase diffusion does not constrain particle growth via condensation of semi-volatile vapours[9].

In addition to confirming the possibility of non-liquid organic PM, the recent laboratory studies further show that physical state varies with a range of factors, ranging from BVOC precursor, to relative humidity (RH), to temperature. The conditions of the boreal forest favour non-liquid PM. By comparison, results of two laboratory studies lead to the hypothesis that liquid PM might prevail over tropical forests[6,7] because of the combination of high isoprene emissions, warm temperatures, and high prevailing RH. Liquids have species diffusivities of the order of 10^{-9} cm^2 s^{-1}.

There are significant uncertainties in the applicability of the laboratory studies to the conditions of tropical forests and hence the viability of the aforementioned hypothesis. Foremost, the laboratory studies produce PM by the oxidation of at most a few BVOC precursors and do so in a simulation chamber. Atmospheric PM is far more complex[20]. It is produced and affected by multiple precursors and pathways, and during its atmospheric lifetime it continues to react with oxidants, sunlight and other species. Thus, in the absence of atmospheric measurements, the physical state of PM over tropical forests remains uncertain, even as these forests and the associated PM cover vast regions of Earth. In this light, in the present study real-world measurements were conducted to test the hypothesis of liquid PM over tropical forests.

At two locations in central Amazonia during the wet and dry seasons, the rebound of sub-micrometre PM was studied using a particle-impaction apparatus equipped with RH adjustment[6,21] (see Methods). Whether or not a particle rebounds is determined by the kinetic energy before impact compared to the sum of dissipation and surface adhesion energies associated with impact[22]. Liquid particles more effectively dissipate energy at impact than do non-liquid particles, and particle adhesion is therefore an indicator of liquid PM. Conversely, the occurrence of particle rebound is an indicator of non-liquid PM. Quantitative calibration of the apparatus was completed using sucrose particles, yielding a viscosity of 10 Pa s as the transition point from rebounding to adhering particles[6].

During the rainy season from 7 to 14 February 2013, PM was sampled at site 'TT34', located 50 km to the north of Manaus, Brazil[23]. During the dry season from 19 to 23 August 2013, PM was

[1]School of Engineering and Applied Sciences, Harvard University, Cambridge, Massachusetts 02138, USA. [2]Federal University of São Carlos, São Paulo 13565-905, Brazil. [3]National Institute of Amazonian Research, Manaus, Amazonas 60060-000, Brazil. [4]University of São Paulo, São Paulo 05508-900, Brazil. [5]Department of Chemistry, University of British Columbia, Vancouver, British Columbia V6T 1Z1, Canada. [6]Department of Earth and Exact Sciences, Federal University of São Paulo, São Paulo 09972-270, Brazil. [7]Amazonas State University, Amazonas 69050-020, Brazil. [8]Pacific Northwest National Laboratory, Richland, Washington 99352, USA. [9]Department of Earth and Planetary Sciences, Harvard University, Cambridge, Massachusetts 02138, USA. *e-mail: scot_martin@harvard.edu

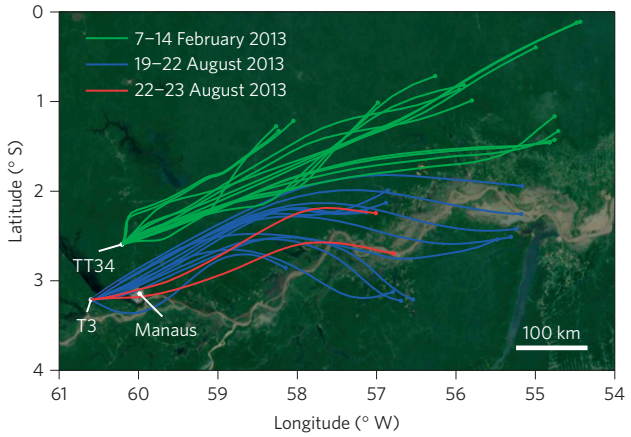

Figure 1 | Locations of the sampling sites TT34 and T3 in relation to the city of Manaus in the central region of the Amazon basin. One-day back trajectories (HYSPLIT model, start height 600 m) are computed for each sampling time at TT34 during 7 to 14 February 2013 (green lines). The one-day back trajectories for T3 during 19 to 23 August 2013 are coloured according to those that pass through the city of Manaus (red lines) and those that do not (blue lines). Image data: Google, Landsat.

sampled at site 'T3', located 60 km to the west of Manaus. For both T3 and TT34, easterlies dominated during the sampling periods. One-day back trajectories at 600 m were calculated for the time of each experiment (Fig. 1 and Supplementary Fig. 1). The air masses sampled at T3 were sometimes affected by the plume of Manaus (red lines of Fig. 1). By comparison, the air masses reaching TT34 (green lines) did not intersect the city during the study period. There was no evidence of significant regional biomass burning during the study periods, although long-range transport and processing of biomass burning material could not be completely ruled out.

The effect of relative humidity on particle rebound is represented in Fig. 2 for all time periods and both measurement sites. The ordinate of the top part of Fig. 2 is the rebound fraction for particles of 200 nm and larger. This size range ensured that the sampled particles had sufficient kinetic energy at impact to overcome the surface adhesion energy (see Supplementary Fig. 2) and that uncertainties in the data analysis were reduced (see Methods). In Fig. 2, an absence of rebound implies liquid PM, as observed at higher RH values. Conversely, a rebound fraction of 0.8 to 1.0 implies non-liquid PM, as observed at lower RH values. The colouring of data points in Fig. 2 associates the different types of back trajectories with the measurements (see Fig. 1). The data show that the transition to liquid PM was complete by 80% RH for clean conditions during both the dry and wet seasons.

This value of 80% RH can be compared to Amazonian climatology. The probability density functions of RH and temperature for the wet and dry seasons of 2014 at T3 are shown in the insets of Fig. 2. The threshold of 80% RH was exceeded 70% and 80% of the time for the dry and wet seasons, respectively. The implication is that the prevailing sub-micrometre PM in Amazonia is liquid most of the time, at least near the Earth's surface. On some hot afternoons in the dry season, the RH drops to as low as 50%, meaning that non-liquid PM might be present at those times, although temperature should also be taken into account as a factor that favours liquid PM during these times. Materials can remain liquid to lower RH for warmer temperatures[24]. Ambient temperatures in the dry season (that is, 300–310 K; see Fig. 2) are largely above the maximum temperature of 300 K of the research trailer in which the RH response was measured.

Organic PM—known to dominate the composition of sub-micrometre PM in this region[23,25–27]—is hygroscopic, and gradual uptake or release of water occurs with changes in relative humidity[28].

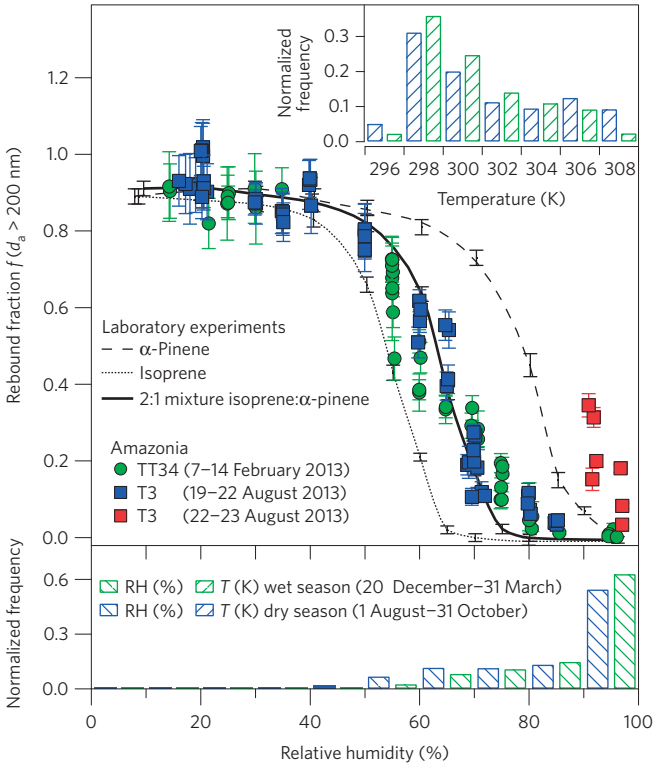

Figure 2 | Rebound fractions of particles having aerodynamic diameters of 200 nm and larger as a function of RH setting. Each data point represents one measurement. Green, red and blue colourings correspond to the back trajectories described in Fig. 1. The one-sigma uncertainty bars are based on error propagation of the condensation particle counters (CPC) measurements and set-point aerodynamic diameter. For comparison to the Amazon data set, data sets are included for PM produced in the Harvard Environmental Chamber from different mixes of BVOCs (ref. 6). The probability density functions of RH and temperature measured at T3 during the 2014 wet (green) and dry (blue) seasons are plotted as insets.

Water is a plasticizer, meaning that it lowers the viscosity of PM (ref. 8). Rebound curves for model PM studied in the laboratory using the same apparatus as in Amazonia are also plotted in Fig. 2 (ref. 6). The rebound curves recorded in Amazonia during clean periods (green and blue symbols) track the general behaviour of the laboratory-generated PM (lines). Figure 2 also shows that the specific behaviour of the diameter of 50% rebound depends on the type of PM produced in the laboratory. PM produced from the oxidation of a mixture of α-pinene and isoprene best reproduces the Amazonian observations. Although Amazonian PM is complex in its origins, isoprene and α-pinene are believed to dominate the long list of BVOC precursors in Amazonia[13,29]. Furthermore, the mass spectrum recorded for Amazonia PM also resembles that of PM produced in the laboratory from these two precursors[27].

On the basis of the laboratory experiments represented in Fig. 2, Bateman *et al.*[6] showed that a hygroscopic growth factor G normalized the RH-dependent rebound curves of the different types of model PM (see Methods). An absorbed water volume of 0.25 ± 0.04, corresponding to $G = 1.10 \pm 0.02$, governed the transition to a liquid state. This relationship is tested herein for the more complex case of PM sampled in Amazonia (see Supplementary Fig. 3). The data of Fig. 2 for clean conditions in both the wet and dry seasons indicates a transition to a liquid state for $G = 1.10 \pm 0.02$, in agreement with the laboratory studies.

These findings suggest that a condition of $G > 1.10 \pm 0.02$ can be used as a heuristic in CTMs for prediction of a liquid state for organic PM. The mechanisms of growth and reactivity prevailing for

different forest types in the absence of pollution can be anticipated, at least for the temperature and composition ranges represented by Fig. 2. Many CTMs already predict G, but do not predict physical state. The implication is that, for times and locations for which the threshold value of G is met, CTMs can assume that particle-phase diffusion does not kinetically limit semi-volatile partitioning of PM. The threshold value of G presented herein can be considered an upper limit, as it corresponds to species diffusivities of the order of 10^{-9} cm^2 s^{-1} (liquid). Diffusion limitations for semi-volatile partitioning are not expected until diffusion coefficients are approximately 10^{-15} cm^2 s^{-1} or lower, corresponding to lower values of G. In the absence of diffusion limitations, other thermodynamic and kinetic factors, most notably particle-phase reactions, can regulate overall gas-particle molecular exchange[30].

The effects of pollution on liquid or non-liquid states of PM remains unknown, including the net effect of soot, inorganic, organic and other constituents in varying quantities. For instance, under urban influence (red symbols of Fig. 2), rebounding particles were observed to 95% RH. Hydrophobic soot, expected to constitute a non-rebounding particle class, is emitted in large quantities from a large fleet of diesel vehicles and other pollution sources in Manaus as well as from brick manufactories to the west of Manaus and along the air mass trajectories of 22 and 23 August. A possibility during these time periods is mixed particles having both liquid and solid components, with a rebound behaviour dominated by the solid component.

The results of the present study highlight a biome-dependent distribution of liquid and non-liquid PM over forested regions. These differences arise both because of intrinsic differences related to BVOC emissions and oxidation pathways as well as extrinsic differences in climatology of RH and temperature, among other possible factors. Boreal forests are dominated by terpene emissions and characterized by low RH (<30% during the sampling period of Virtanen *et al.*[5]). The results plotted in Fig. 2 suggest that non-liquid PM should be anticipated for these conditions. By comparison, tropical forests are dominated by isoprene emissions, and high RH (>80%) prevails. In consequence (Fig. 2), sub-micrometre PM is primarily in a liquid form over the Amazon rainforest.

Methods

Methods and any associated references are available in the online version of the paper.

Received 15 May 2015; accepted 15 October 2015; published online 7 December 2015

References

1. Ramanathan, V., Crutzen, P. J., Kiehl, J. T. & Rosenfeld, D. Atmosphere-aerosols, climate, and the hydrological cycle. *Science* **294**, 2119–2124 (2001).
2. Kuwata, M. & Martin, S. T. Phase of atmospheric secondary organic material affects its reactivity. *Proc. Natl Acad. Sci. USA* **109**, 17354–17359 (2012).
3. Perraud, V. *et al*. Nonequilibrium atmospheric secondary organic aerosol formation and growth. *Proc. Natl Acad. Sci. USA* **109**, 2836–2841 (2012).
4. Andreae, M. O. & Rosenfeld, D. Aerosol–cloud–precipitation interactions. Part 1. The nature and sources of cloud-active aerosols. *Earth Sci. Rev.* **89**, 13–41 (2008).
5. Virtanen, A. *et al*. An amorphous solid state of biogenic secondary organic aerosol particles. *Nature* **467**, 824–827 (2010).
6. Bateman, A. P., Bertram, A. K. & Martin, S. T. Hygroscopic influence on the semisolid-to-liquid transition of secondary organic materials. *J. Phys. Chem. A* **119**, 4386–4395 (2015).
7. Song, M. *et al*. Relative humidity-dependent viscosities of isoprene-derived secondary organic material and atmospheric implications for isoprene-dominant forests. *Atmos. Chem. Phys.* **15**, 5145–5159 (2015).
8. Koop, T., Bookhold, J., Shiraiwa, M. & Poschl, U. Glass transition and phase state of organic compounds: Dependency on molecular properties and implications for secondary organic aerosols in the atmosphere. *Phys. Chem. Chem. Phys.* **13**, 19238–19255 (2011).
9. Riipinen, I. *et al*. The contribution of organics to atmospheric nanoparticle growth. *Nature Geosci.* **5**, 453–458 (2012).
10. Riipinen, I. *et al*. Organic condensation: A vital link connecting aerosol formation to cloud condensation nuclei (CCN) concentrations. *Atmos. Chem. Phys.* **11**, 3865–3878 (2011).
11. Murray, B. J. *et al*. Heterogeneous nucleation of ice particles on glassy aerosols under cirrus conditions. *Nature Geosci.* **3**, 233–237 (2010).
12. Jimenez, J. L. *et al*. Evolution of organic aerosols in the atmosphere. *Science* **326**, 1525–1529 (2009).
13. Martin, S. T. *et al*. Sources and properties of Amazonian aerosol particles. *Rev. Geophys.* **48**, RG2002 (2010).
14. Shiraiwa, M., Ammann, M., Koop, T. & Poschl, U. Gas uptake and chemical aging of semisolid organic aerosol particles. *Proc. Natl Acad. Sci. USA* **108**, 11003–11008 (2011).
15. Zaveri, R. A., Easter, R. C., Shilling, J. E. & Seinfeld, J. H. Modeling kinetic partitioning of secondary organic aerosol and size distribution dynamics: Representing effects of volatility, phase state, and particle-phase reaction. *Atmos. Chem. Phys.* **14**, 5153–5181 (2014).
16. Vaden, T. D. *et al*. Evaporation kinetics and phase of laboratory and ambient secondary organic aerosol. *Proc. Natl Acad. Sci. USA* **108**, 2190–2195 (2011).
17. Renbaum-Wolff, L. *et al*. Viscosity of α-pinene secondary organic material and implications for particle growth and reactivity. *Proc. Natl Acad. Sci. USA* **110**, 8014–8019 (2013).
18. Kidd, C., Perraud, V., Wingen, L. M. & Finlayson-Pitts, B. J. Integrating phase and composition of secondary organic aerosol from the ozonolysis of α-pinene. *Proc. Natl Acad. Sci. USA* **111**, 7552–7557 (2014).
19. Shiraiwa, M., Zuend, A., Bertram, A. K. & Seinfeld, J. H. Gas-particle partitioning of atmospheric aerosols: Interplay of physical state, non-ideal mixing and morphology. *Phys. Chem. Chem. Phys.* **15**, 11441–11453 (2013).
20. Hallquist, M. *et al*. The formation, properties and impact of secondary organic aerosol: Current and emerging issues. *Atmos. Chem. Phys.* **9**, 5155–5236 (2009).
21. Bateman, A. P., Belassein, H. & Martin, S. T. Impactor apparatus for the study of particle rebound: Relative humidity and capillary forces. *Aerosol Sci. Technol.* **48**, 42–52 (2014).
22. Tsai, C. J., Pui, D. Y. H. & Liu, B. Y. H. Capture and rebound of small particles upon impact with solid-surfaces. *Aerosol Sci. Technol.* **12**, 497–507 (1990).
23. Martin, S. T. *et al*. An overview of the Amazonian Aerosol Characterization Experiment 2008 (AMAZE-08). *Atmos. Chem. Phys.* **10**, 11415–11438 (2010).
24. Wang, B. *et al*. Reactivity of liquid and semisolid secondary organic carbon with chloride and nitrate in atmospheric aerosols. *J. Phys. Chem. A* **119**, 4498–4508 (2015).
25. Chen, Q. *et al*. Mass spectral characterization of submicron biogenic organic particles in the Amazon basin. *Geophys. Res. Lett.* **36**, L20806 (2009).
26. Poschl, U. *et al*. Rainforest aerosols as biogenic nuclei of clouds and precipitation in the Amazon. *Science* **329**, 1513–1516 (2010).
27. Chen, Q. *et al*. Submicron particle mass concentrations and sources in the Amazonian wet season (AMAZE-08). *Atmos. Chem. Phys.* **15**, 3687–3701 (2015).
28. Varutbangkul, V. *et al*. Hygroscopicity of secondary organic aerosols formed by oxidation of cycloalkenes, monoterpenes, sesquiterpenes, and related compounds. *Atmos. Chem. Phys.* **6**, 2367–2388 (2006).
29. Claeys, M. *et al*. Formation of secondary organic aerosols through photooxidation of isoprene. *Science* **303**, 1173–1176 (2004).
30. Kalberer, M. *et al*. Identification of polymers as major components of atmospheric organic aerosols. *Science* **303**, 1659–1662 (2004).

Acknowledgements

Institutional support was provided by the Central Office of the Brazil Large-Scale Biosphere Atmosphere Experiment in Amazonia (LBA) and the Brazil National Institute of Amazonian Research (INPA). We acknowledge the Atmospheric Radiation Measurement (ARM) Climate Research Facility, a user facility of the United States Department of Energy, Office of Science, sponsored by the Office of Biological and Environmental Research, and support from the Atmospheric System Research (ASR) Program of that office. Funding was obtained from the United States Department of Energy (DOE), the São Paulo Research Foundation (FAPESP), the Amazonas State Research Foundation (FAPEAM), and the Brazil Scientific Mobility Program (CsF/CAPES). The authors acknowledge the Air Resources Laboratory of the United States National Oceanic and Atmospheric Administration (NOAA) for the provision of the website http://www.ready.noaa.gov for use of HYSPLIT. The research described herein was conducted under scientific licence 001030/2012-4 of the Brazilian National Council for Scientific and Technological Development (CNPq). Y. Ishida and B. Takeshi are gratefully acknowledged for logistical support of the measurements.

Author contributions

A.P.B. carried out measurements, processed and analysed data, and contributed to the writing. P.L., Y.Z., B.S. and G.C. aided in the measurements. Z.G. participated in data analysis. A.O.M., P.A. and R.A.F.S. served in leadership roles for the infrastructure of the measurements. P.A., A.K.B., L.V.R. and R.A.Z. contributed to interpretation and writing. S.T.M. served as principal investigator of the project and contributed to data analysis, interpretation, and writing.

Additional information

Supplementary information is available in the online version of the paper. Reprints and permissions information is available online at www.nature.com/reprints. Correspondence and requests for materials should be addressed to S.T.M.

Competing financial interests

The authors declare no competing financial interests.

Methods

Site location. At TT34 (2° 35′ 40.50″ S, 60° 12′ 33.42″ W) during the wet season of 2013, PM was sampled from the top of a tower at a height of 39 m, brought to ground level through tubing (passing particles of 4 nm to 7 µm), and dried to 35 to 40% RH. Instrumentation was housed inside an air-conditioned research trailer at tower base. TT34 is located in a terra firma forest having a canopy near 35 m. At T3 (3° 12′ 47.82″ S, 60° 35′ 55.32″ W) during the dry season of 2013, a single air-conditioned trailer equipped with a sampling mast at 6 m was located in a pasture site. Particles passed through a diffusion dryer (50% RH). For the prevailing easterlies, the forest was 2 km from T3. This pasture site was later extensively developed for the GoAmazon2014/5 Experiment[31], and data sets of temperature and RH were continuously collected across the dry and wet seasons of 2014. The TT34 site is also referred to as 'T0t' in GoAmazon2014/5 and 'ZF2' in other literature.

Measurement technique. The impactor apparatus used herein was designed for the study of particle rebound of sub-micrometre particles. The design of each individual impactor followed prevailing literature guidelines[32,33]. Although particle rebound has been known for many years[34,35], only recently has it emerged as a technique to probe the physical state of particles[5].

At both T3 and TT34, the PM was sampled by an impactor apparatus housed inside the research trailers[6,21]. The apparatus consisted of an initial drying unit (TSI 3062) to <25% RH, a differential mobility analyzer (DMA, TSI 3085) to select dry particles by electric mobility, Nafion tubes (Perma Pure, MD 110) to re-humidify particles to a variable RH up to 96%, three impactors in a parallel-arm configuration, and condensation particle counters (CPC, TSI 3010) to measure the particle number concentration N transmitted through each impaction arm. The set-point aerodynamic diameter d_a^* of the impactors was 84.9 ± 5.4 nm (one sigma) at a flow rate of $1.0\,l\,m^{-1}$. The data protocol was to fix RH and to increase stepwise the mobility diameter every 2 min. In this way, one experiment was completed every 60–90 min at a fixed RH. The three different impactors represented configurations having an uncoated aluminium impaction plate N_i, an impaction plate coated with high-vacuum grease (Dow Corning) N_{ii}, and an absence of an impaction plate N_{iii}.

Data analysis: transmission function. The transmission functions $\Omega_{uncoated}$ and Ω_{coated} for the uncoated and coated arms, respectively, were calculated as follows[21]:

$$\Omega_{uncoated} = \frac{N_i}{N_{iii}}, \quad \Omega_{coated} = \frac{N_{ii}}{N_{iii}} \tag{1}$$

from particle number concentrations N measured by three condensation particle counters. The standard deviation of each transmission function was based on error propagation using an uncertainty estimate of $N^{-1/2}$ (ref. 36).

The full set of transmission functions $\Omega_{coated}(d_m)$ and $\Omega_{uncoated}(d_m)$, as measured by stepwise adjustments of the mobility diameter d_m selected by the DMA, are shown in Supplementary Figs 4 and 5. The figures show results for the wet and dry seasons, respectively. A sigmoid function represents the transmission function of a well-designed impactor, as follows:

$$\Omega(d_m) = \frac{1}{1+\exp((d_m - d_m^*)/\delta)} \tag{2}$$

for a set-point diameter d_m^* and a width parameter δ. The values of $d_{m,i}^*$ and δ_i, as well as the one-sigma uncertainties for each parameter, are listed in Supplementary Table 1 for each experiment i. The fitted sigmoid functions are shown as dashed lines in Supplementary Figs 4 and 5. Small shoulders that do not match the fits arise from multiply charged particles that pass through the DMA. These data points are not included in the fitting. The goodness of fit parameter χ^2 is listed in Supplementary Table 1.

The data sets of $\Omega_{coated}(d_m)$ and $\Omega_{uncoated}(d_m)$ were converted to data sets of $\Omega_{coated}(d_a)$ and $\Omega_{uncoated}(d_a)$ by calculating aerodynamic diameter from mobility diameter, as follows:

$$d_a = \left(\frac{\rho_p}{\rho_0}\frac{C_c(d_m)}{C_c(d_a)}\right)^{1/2} d_m \tag{3}$$

This equation is for a limiting assumption of non-porous spherical particles having +1 charge[37]. Terms include the particle material density ρ_p, a reference material density ρ_0 (1,000 kg m^{-3}), and the Cunningham slip correction factors $C_c(d_m)$ and $C_c(d_a)$. The material density $\rho_{p,i}$ of the different data sets i depended on relative humidity (see Data analysis: material density and growth factor). The full set of transmission functions $\Omega_{coated}(d_a)$ and $\Omega_{uncoated}(d_a)$ is shown in Supplementary Figs 6 and 7.

An empirical translation to the abscissa of each data set was made to compensate for minor manufacturing differences among nozzle plates, differences in experimental temperature and flow compared to calibration, and the variability in grease coating on local flow patterns compared to calibration[6,21]. The coated data sets were individually translated along the abscissa so that the transmission function $\Omega_{coated}(d_a)$ was 0.5 at 84.9 nm, corresponding to the calibrated set-point diameter d_a^* of the apparatus. The uncoated data sets were individually translated along the abscissa so that $\Omega_{uncoated}(d_a)$ equalled $\Omega_{coated}(d_a)$ at the onset of particle rebound. The onset of particle rebound was determined by visual inspection of each data set. The magnitudes of the translations are listed in Supplementary Table 2 for each data set. The full sets of shifted transmission functions $\Omega_{coated}(d_a)$ and $\Omega_{uncoated}(d_a)$ are shown in Supplementary Figs 8 and 9.

Data analysis: rebound fraction. The rebound fraction was calculated from the shifted transmission functions $\Omega_{coated}(d_a)$ and $\Omega_{uncoated}(d_a)$, as follows:

$$f(d_a) = \frac{\Omega_{uncoated}(d_a) - \Omega_{coated}(d_a)}{1 - \Omega_{coated}(d_a)} = \frac{N_i/N_{iii} - N_{ii}/N_{iii}}{1 - N_{ii}/N_{iii}} \tag{4}$$

Because of the translations, the abscissa values of the measured $\Omega_{coated}(d_a)$ and $\Omega_{uncoated}(d_a)$ were not in registry. In this case, $\Omega_{coated}(d_a)$ was well fitted to a version of equation (2) (that is, using d_a in place of d_m) to facilitate application of equation (4) (that is, discrete values of $\Omega_{uncoated}(d_a)$ and continuous values of $\Omega_{coated}(d_a)$). The full sets of calculated rebound fractions are shown in Supplementary Figs 10 and 11.

Data analysis: material density and growth factor. In comparison to the earlier analysis of laboratory data sets for which the particle material density ρ_p was known a priori[6,21], the analysis presented herein of atmospheric data sets required an estimate of ρ_p to apply equation (3). The density was assumed to follow a volume mixing rule between $\rho_{p,dry}$ of the organic material and $\rho_{p,water}$ of water[38]. The fractional particle water volume was derived by assuming the following relationship[39]:

$$G = \left[1 + \left(\frac{RH/100}{1 - RH/100}\right) A\right]^{1/3} \tag{5}$$

In this equation, G is the diameter-based hygroscopic growth factor, RH is relative humidity, and A is an empirical hygroscopicity parameter.

Values of $\rho_{p,dry}$ and A, as needed to estimate $\rho_{p,i}$ of each experiment, were obtained by global optimization to each seasonal data set. The minimized quantity was $\sum_i (d_{a,i}^* - d_{a,0}^*)^2$ for each season, for which $d_{a,0}^* = 84.9$ nm. For each i, $d_{a,i}^*$ was obtained using equation (3) with parameter values of $d_{m,i}^*$ listed in Supplementary Table 1 and $\rho_{p,i}(\rho_{p,dry}, A)$ obtained by the volume mixing rule. Values of $\rho_{p,dry}$ and A were taken as constant within one season. The optimized values of $\rho_{p,dry}$ were 1,390 kg m^{-3} and 1,290 kg m^{-3} for the wet and dry seasons, respectively. Previous studies in Amazonia during the wet[27] and dry[39] seasons reported respective densities of 1,390 kg m^{-3} and 1,350 kg m^{-3}. The optimized values of A were 0.053 and 0.063 for the wet and dry seasons, respectively. Previously, values of A ranging from 0.044 to 0.065 were reported for Amazonia[39]. For reference, for the stated optimized values of A, the corresponding hygroscopic growth factors at 90% RH were 1.14 and 1.16, respectively. Previously, hygroscopic growth factors at 90% RH have been reported to range from 1.12 to 1.17 (ref. 39).

Diameter-dependent rebound curve. Supplementary Fig. 2 shows one example of diameter-dependent rebound observed at TT34 for four RH values, expressed as the rebound fraction $f(d_a)$ for aerodynamic diameter d_a. The full sets of data collected at both TT34 and T3 are given in the Supplementary Figs 4 to 11. For a single RH value, the rebound curve can be analysed in three segments, defined by the set-point aerodynamic diameter d_a^*, along the diameter abscissa. For the first segment, $d_a \ll d_a^*$, the rebound fraction is zero (left of dashed line). For the second segment, $d_a \approx d_a^*$, the rebound fraction steadily increases with d_a for non-liquid particles or remains zero for liquid particles. For the third segment, $d_a \gg d_a^*$, the rebound fraction obtains a limiting value that depends only weakly on d_a (refs 6,21).

The behaviour in each of these three segments is explained by the energetics of particle–surface interactions at impact[21]. For segment 1, the incoming particle kinetic energy is less than the surface adhesion energy, implying that rebound does not occur. For segment 2, the fraction of particles having a kinetic energy greater than the surface adhesion energy steadily increases with diameter, meaning that the rebound fraction steadily increases for non-liquid PM. For liquid PM, additional mechanisms of energy dissipation such as particle flattening are available on impact, and complete adhesion occurs for both segments 2 and 3. For the non-liquid PM of segment 3, the maximum rebound fraction is achieved because all particles have a kinetic energy greater than the surface adhesion energy.

Supplementary Fig. 2 shows that the rebound behaviour depends strongly on RH. The RH is adjusted stepwise during the course of a measurement. Water is a plasticizer, meaning that it lowers the viscosity of PM (ref. 8). The data in Supplementary Fig. 2 implicate non-liquid PM at 25% RH and liquid PM at 95%

RH. At 75% RH, some particles rebound whereas others do not because of the distribution in particle kinetic energy across the flow streamlines of the impactor[21]. These particles have lower viscosities but are not yet liquid.

Data sets. The data sets corresponding to the figures and tables are included in the Supplementary Information as ASCII text files (PDF attachments).

References

31. Martin, S. T. *et al*. Introduction: Observations and modeling of the green ocean Amazon (GoAmazon2014/5). *Atmos. Chem. Phys. Discuss.* **15**, 30175–30210 (2015).
32. Hinds, W. C. *Aerosol Technology: Properties, Behavior, and Measurement of Airborne Particles* 2nd edn (Wiley, 1999).
33. Marple, V. A. & Willeke, K. Impactor design. *Atmos. Environ.* **10**, 891–896 (1976).
34. Dahneke, B. The capture of aerosol particles by surfaces. *J. Colloid Interface Sci.* **37**, 342–353 (1971).
35. Winkler, P. Relative humidity and the adhesion of atmospheric particles to the plates of impactors. *J. Aerosol Sci.* **5**, 235–240 (1974).
36. Agarwal, J. K. & Sem, G. J. Continuous flow, single-particle-counting condensation nucleus counter. *J. Aerosol Sci* **11**, 343–357 (1980).
37. Kelly, W. P. & McMurry, P. H. Measurement of particle density by inertial classification of differential mobility analyzer generated monodisperse aerosols. *Aerosol Sci. Technol.* **17**, 199–212 (1992).
38. Brechtel, F. J. & Kreidenweis, S. M. Predicting particle critical supersaturation from hygroscopic growth measurements in the humidified TDMA. Part I: Theory and sensitivity studies. *J. Atmos. Sci.* **57**, 1854–1871 (2000).
39. Rissler, J. *et al*. Size distribution and hygroscopic properties of aerosol particles from dry-season biomass burning in Amazonia. *Atmos. Chem. Phys.* **6**, 471–491 (2006).

nature geoscience

SUPPLEMENTARY INFORMATION

DOI: 10.1038/NGEO2599

Sub-micrometre particulate matter is primarily in liquid form over Amazon rainforest

Adam P. Bateman, Zhaoheng Gong, Pengfei Liu, Bruno Sato, Glauber Cirino, Yue Zhang, Paulo Artaxo, Allan K. Bertram, Antonio O. Manzi, Luciana V. Rizzo, Rodrigo A. F. Souza, Rahul A. Zaveri, Scot T. Martin*

* Correspondence to: S.T. Martin (scot_martin@harvard.edu)

Wet Season					
i	Date and Time	RH	$d^*_{m,i}$	δ_i	χ^2
1	07 Feb 2013 18:14	20	61.9 ± 2.2 nm	16.7 ± 2.4	0.02
2	07 Feb 2013 19:01	50	62.3 ± 2.2	13.7 ± 2.4	0.03
3	10 Feb 2013 18:05	85	65.9 ± 0.7	10.3 ± 0.7	0.02
4	10 Feb 2013 19:53	65	64.4 ± 1.2	11.3 ± 1.6	0.02
5	11 Feb 2013 14:00	15	65.1 ± 1.3	13.6 ± 1.5	0.04
6	11 Feb 2013 15:32	35	63.0 ± 0.8	11.7 ± 1.0	0.01
7	11 Feb 2013 17:06	70	64.5 ± 0.8	8.3 ± 0.8	0.04
8	12 Feb 2013 12:58	30	62.6 ± 2.0	16.8 ± 2.3	0.11
9	13 Feb 2013 16:05	95	56.3 ± 0.5	6.5 ± 0.4	0.02
10	13 Feb 2013 17:42	75	57.3 ± 1.8	12.3 ± 1.9	0.13
11	13 Feb 2013 20:33	55	62.3 ± 1.7	13.7 ± 2.3	0.01
12	14 Feb 2013 13:16	25	70.8 ± 0.8	11.6 ± 0.8	0.02
13	14 Feb 2013 14:57	55	64.3 ± 1.3	13.3 ± 1.3	0.06
14	14 Feb 2013 16:31	60	65.5 ± 0.9	11.3 ± 0.9	0.03
15	14 Feb 2013 18:02	80	63.9 ± 0.6	9.3 ± 0.6	0.03
Dry Season					
i	Date and Time	RH	$d^*_{m,i}$	δ_i	χ^2
16	19 Aug 2013 22:50	15	63.5 ± 2.3 nm	16.6 ± 2.7	0.01
17	20 Aug 2013 16:17	30	79.9 ± 0.9	14.4 ± 1.0	0.01
18	20 Aug 2013 18:41	50	65.6 ± 2.4	14.9 ± 2.8	0.02
19	20 Aug 2013 20:23	70	62.6 ± 2.3	14.2 ± 2.1	0.10
20	21 Aug 2013 13:16	20	64.9 ± 2.4	15.4 ± 2.3	0.08
21	21 Aug 2013 15:08	40	68.7 ± 1.6	14.5 ± 1.9	0.01
22	21 Aug 2013 17:04	60	64.0 ± 2.7	17.4 ± 2.7	0.09
23	21 Aug 2013 19:03	80	61.4 ± 2.4	12.6 ± 2.3	0.09
24	21 Aug 2013 20:52	70	64.6 ± 1.2	10.1 ± 1.1	0.03
25	22 Aug 2013 13:54	20	71.3 ± 6.3	9.7 ± 5.9	0.90
26	22 Aug 2013 15:49	85	60.4 ± 1.2	12.0 ± 1.2	0.02
27	22 Aug 2013 17:33	65	66.0 ± 3.3	16.6 ± 3.4	0.13
28	22 Aug 2013 19:17	35	69.0 ± 2.1	12.6 ± 2.0	0.07
29	22 Aug 2013 21:01	90	60.7 ± 2.2	16.0 ± 2.2	0.05
30	23 Aug 2013 22:27	96	62.9 ± 1.2	12.7 ± 1.2	0.02

Table S1. The value $d^*_{m,i}$ of each experiment i is obtained by fitting the experimental data to Equation M2. See further explanation in Section M3. The one-sigma uncertainties represent the standard deviation obtained from fitting. The goodness of fit parameter χ^2 is also listed. The timestamps represent UTC. Local time in Manaus is -4 h compared to UTC.

Wet Season	Coated		Uncoated	
07 Feb 2013 18:14	+3.2 nm	+3.8 %	-24.4 nm	-28.7 %
07 Feb 2013 19:01	+2.3	+2.7	-14.4	-17.0
10 Feb 2013 18:05	-4.4	-5.2	+2.2	+2.7
10 Feb 2013 19:53	-0.8	-1.0	-2.4	-2.8
11 Feb 2013 14:00	-1.0	-1.2	-24.2	-28.5
11 Feb 2013 15:32	2.8	+3.3	-23.9	-28.2
11 Feb 2013 17:06	-1.1	-1.3	-13.8	-16.2
12 Feb 2013 12:58	+2.1	+2.5	-23.2	-27.3
13 Feb 2013 16:05	+2.5	+3.0	+5.7	+6.7
13 Feb 2013 17:42	+7.9	+9.3	-0.1	-0.1
13 Feb 2013 20:33	+2.2	+2.6	-19.1	-22.4
14 Feb 2013 13:16	-8.2	-9.4	-17.0	-20.0
14 Feb 2013 14:57	-0.3	-0.4	-18.7	-22.0
14 Feb 2013 16:31	-2.0	-2.4	-15.3	-18.0
14 Feb 2013 18:02	-2.0	-2.4	-1.2	-1.4
Dry Season				
19 Aug 2013 22:50	+6.1 nm	+7.2 %	-22.2 nm	-26.2 %
20 Aug 2013 16:17	-13.6	-16.0	-27.9	-32.9
20 Aug 2013 18:41	+2.9	+3.4	-9.6	-11.4
20 Aug 2013 20:23	+5.8	+6.8	+7.6	+8.9
21 Aug 2013 13:16	+4.4	+5.2	-22.0	-25.9
21 Aug 2013 15:08	-0.6	-0.7	-21.7	-25.6
21 Aug 2013 17:04	+3.6	+4.2	-4.5	-5.4
21 Aug 2013 19:03	+6.1	+7.2	+1.5	+1.7
21 Aug 2013 20:52	+3.2	+3.8	-9.4	-11.1
22 Aug 2013 13:54	-2.0	-2.4	-12.8	-15.1
22 Aug 2013 15:49	+6.1	+7.2	+1.3	+1.5
22 Aug 2013 17:33	+2.0	+2.4	-6.0	-7.1
22 Aug 2013 19:17	-0.8	-0.9	-10.5	-12.4
22 Aug 2013 21:01	+3.6	+4.2	-10.0	-11.8
23 Aug 2013 22:27	-8.6	-10.1	-13.4	-15.8

Table S2. Empirical translations of the original data sets along the abscissa to adjust measurements to the apparatus setpoint diameter d_a^* of 84.9 nm. See Section M3 for further explanation. Results are listed for the transmission functions of both the coated and uncoated impactor plates. The timestamps represent UTC. Local time in Manaus is -4 h compared to UTC.

List of Supplementary Figures

Figure S1. Back trajectories calculated for the measurements at TT34 and T3. One-day back trajectories[40] (HYSPLIT model, NOAA-ARL, start height 600 m) computed for TT34 are traced using green lines. The one-day back trajectories computed for T3 are traced using red for those that pass through the city of Manaus or blue for those that do not. The numbering of each back trajectory corresponds to numbering of each diameter-resolved measurement.

Figure S2. Diameter-resolved rebound fraction $f(d_a)$ measured at TT34 during the wet season. The datasets, collected during the daytime of 13 and 14 Feb 2013, correspond to Experiments 9 to 12 of Table S1. Data points are colored by the RH setting. The one-sigma uncertainty bars are based on error propagation of the CPC measurements and set-point aerodynamic diameter. The dashed vertical line indicates the setpoint aerodynamic diameter d_a^* of the impactor for the employed flows. Figures S10 and S11 show the data sets for all experiments. Measurement temperatures ranged from 296 to 300 K during the period of measurements.

Figure S3. Rebound fractions of particles having aerodynamic diameters of 200 nm and larger. Data are plotted by G (cf. Section M5). For comparison, data sets are also shown for different types of PM produced in the Harvard Environmental Chamber[41,42]. Green, red, and blue colorings correspond to the back trajectories described in Figure 1. The one-sigma uncertainty bars are based on error propagation of the CPC measurements.

Figure S4. The diameter-resolved transmission functions $\Omega(d_m)$ as measured in mobility diameter. Data were collected at TT34 during the wet season (Feb 2013). Each

panel represents a set of measurements conducted at a specific RH. The measurement temperature is also listed. The solid circles represent $\Omega_{uncoated}(d_m)$ for uncoated impactor plates (cf. Equation M1). The open circles represent $\Omega_{coated}(d_m)$ for coated impactor plates. The dashed line represents the fit to $\Omega_{coated}(d_m)$ using Equation M2. The one-sigma uncertainty bars are based on error propagation of the CPC measurements.

Figure S5. As for Figure S4 but for measurements during the dry season.

Figure S6. The diameter-resolved transmission functions $\Omega(d_a)$ once converted to aerodynamic diameter (cf. Equation M3). The solid circles represent $\Omega_{uncoated}(d_a)$ for uncoated impactor plates. The open circles represent $\Omega_{coated}(d_a)$ for coated impactor plates. The one-sigma uncertainty bars are based on error propagation of the CPC measurements. In these panels, there is no adjustment of the abscissa (cf. Figure S8). The data are for the wet season, and the panels correspond to those shown in Figure S4.

Figure S7. As for Figure S6 but for measurements during the dry season (Aug 2013). The panels correspond to those shown in Figure S5.

Figure S8. Diameter-resolved transmission functions $\Omega(d_a)$ after translation of the data sets along the abscissa. The adjustment compensates for variations in flow and coating thickness among experiments (cf. Table S2). See text for a further explanation of the abscissa adjustment. The data are for the wet season, and the panels correspond to those shown in Figure S4.

Figure S9. As for Figure S8 but for measurements during the dry season. The panels correspond to those shown in Figure S5.

Figure S10. Diameter-resolved rebound fraction $f(d_a)$ for PM sampled during the wet season (cf Equation M4). Data are color-coded by back trajectory according to the conventions of Figure 1. The numbering corresponds to the back trajectories of Figure S1 as well as the experiment numbers of Table S1. The presented timestamps are for UTC. Local time in Manaus is -4 h compared to UTC. The data are for the wet season, and the panels correspond to those shown in Figure S4. The one-sigma uncertainty bars are based on error propagation of the CPC measurements and set-point aerodynamic diameter.

Figure S11. As for Figure S10 but for measurements during the dry season. The data are for the wet season, and the panels correspond to those shown in Figure S5.

References

40 *HYSPLIT (HYbrid Single-Particle Langrangian Integrated Trajectory) Model access via NOAA ARL READY website (http://www.arl.noaa.gov/HYSPLIT_info.php)* (NOAA Air Resources Laboratory, College Park, MD), 2015.

41 King, S. M. *et al.* Increased cloud activation potential of secondary organic aerosol for atmospheric mass loadings. *Atmos. Chem. Phys.* **9**, 2959-2971 (2009).

42 Shilling, J. E. *et al.* Particle mass yield in secondary organic aerosol formed by the dark ozonolysis of alpha-pinene. *Atmos. Chem. Phys.* **8**, 2073-2088 (2008).

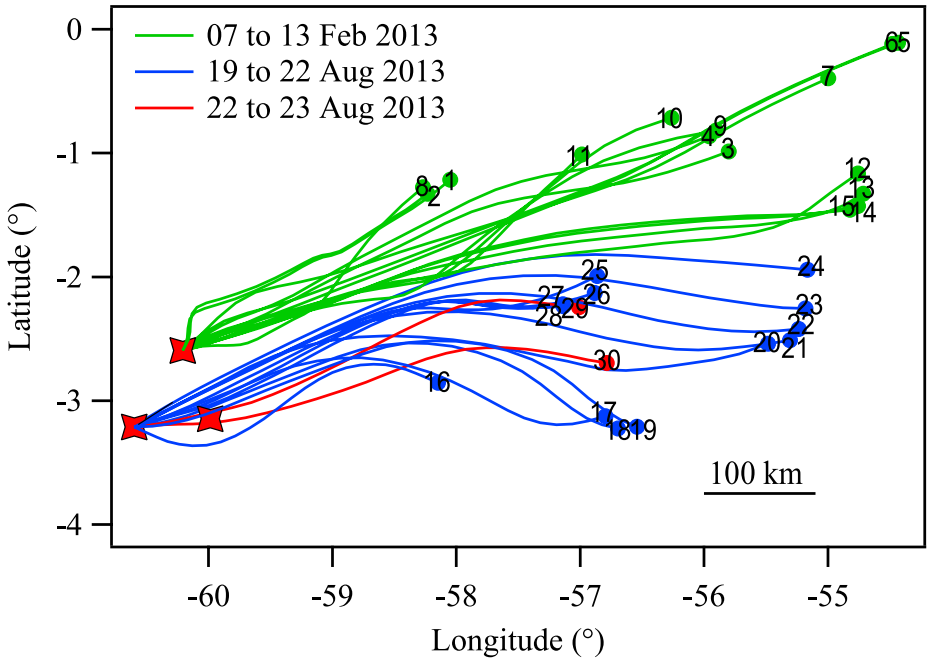

Figure S1

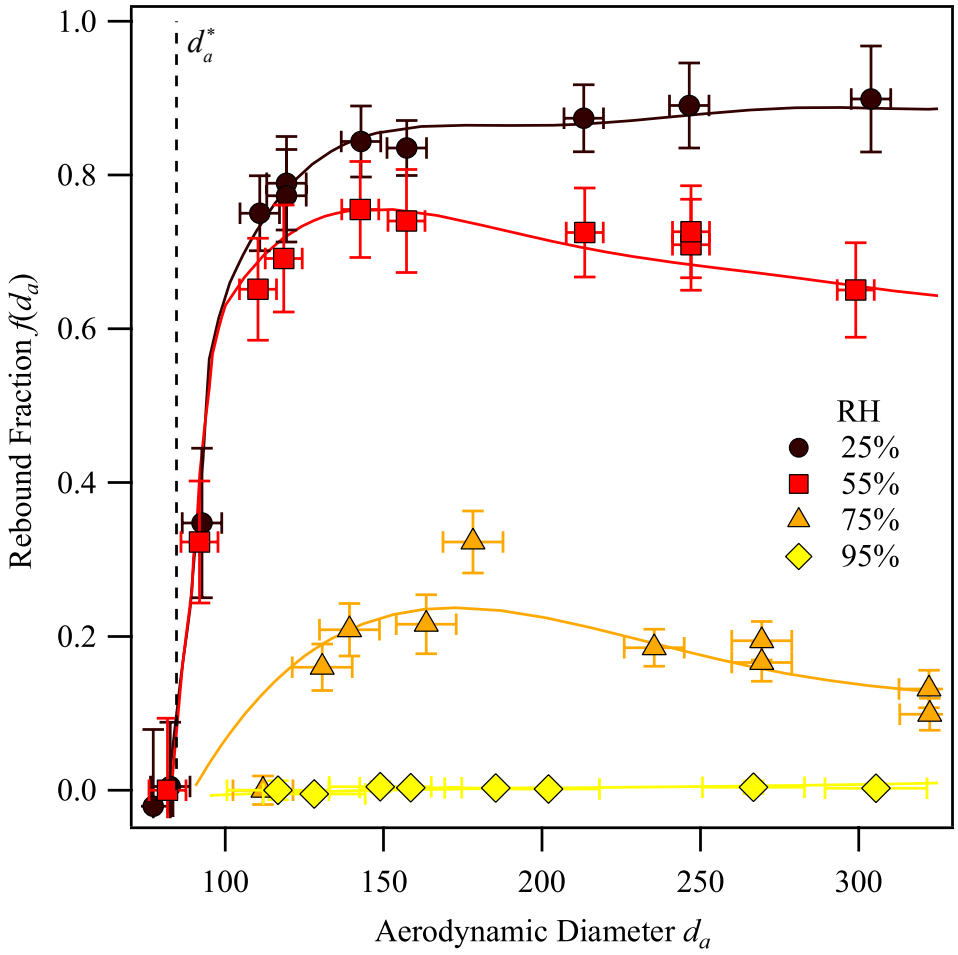

Figure S2

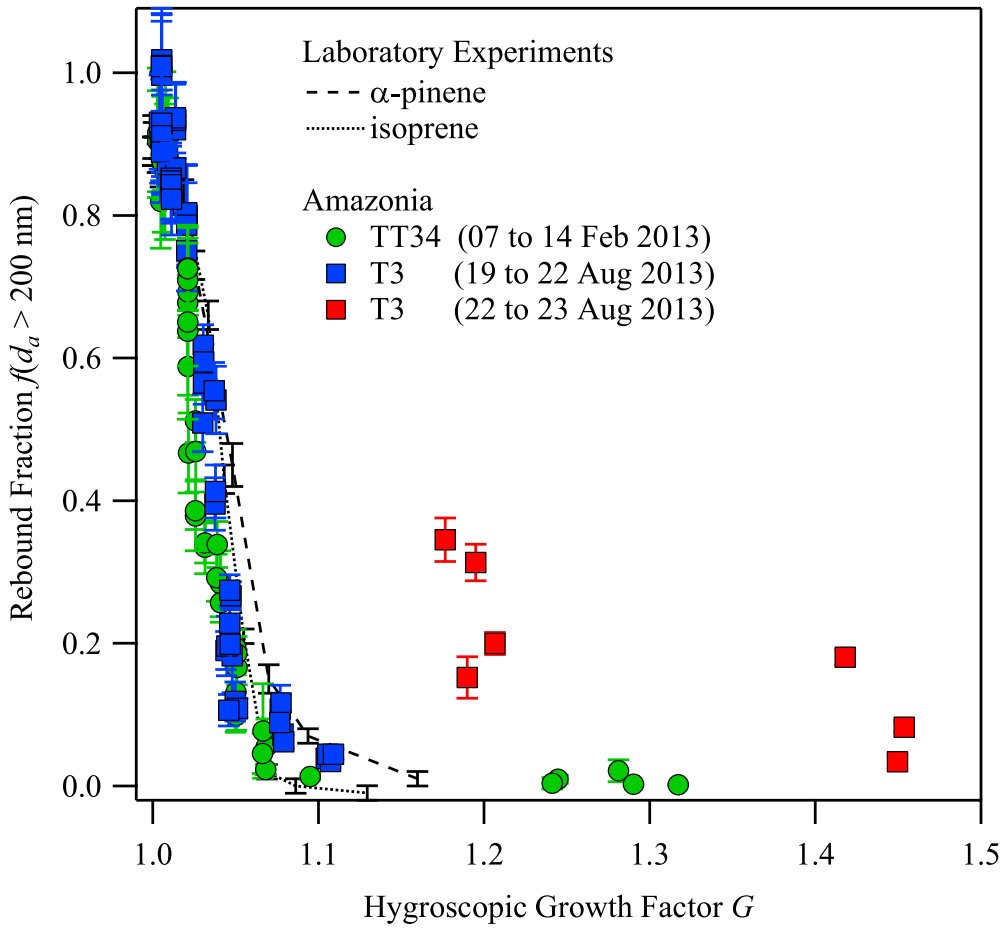

Figure S3